Results in Engineering 28 (2025) 108085

Contents lists available at ScienceDirect

Results in Engineering

journal homepage: www.sciencedirect.com/journal/results-in-engineering

Thermal analysis for magneto- Carreau based ternary hybrid nanofluids over stretchable surfaces under convective conditions

Imran Ullah [a], Waqar A. Khan [b,c], Maimoona Karim [d,*], Syed M. Hussain [e], Hijaz Ahmad [e,f,g,h,i], Wasim Jamshed [b,j,k], Siti Suzilliana Putri Mohamed Isa [l,m]

[a] College of Civil Engineering, National University of Sciences and Technology, Islamabad 44000, Pakistan
[b] Department of Mathematics, Saveetha School of Engineering, SIMATS, Saveetha University, Chennai 602105, Tamil Nadu, India
[c] Applied Science Research Center, Applied Science Private University, Al-Arab St. Amman, Jordan
[d] Department of Mathematics, University of Education Lahore, D.G. Khan Campus, Pakistan
[e] Department of Mathematics, Faculty of Science, Islamic University of Madinah, Madinah, 42351, Saudi Arabia
[f] Operational Research Center in Healthcare, Near East University, Mersin 10, Nicosia, 99138 TRNC, Turkey
[g] VIZJA University, Okopowa 59, Warsaw, 01-043, Poland
[h] Department of Mathematics, College of Science, Korea University, 145 Anam-ro, Seongbuk-gu, Seoul, 02841, South Korea
[i] Engineered Biomaterials Research Center, Khazar University, Baku, Azerbaijan
[j] Department of Mathematics, Capital University of Science and Technology (CUST), Islamabad, 44000, Pakistan
[k] Department of Computer Engineering, Biruni University, Topkapi, Istanbul, Turkey
[l] Institute for Mathematical Research, Universiti Putra Malaysia, 43400 UPM Serdang, Selangor, Malaysia
[m] Centre of Foundation Studies in Science of Universiti Putra Malaysia, Universiti Putra Malaysia, 43400 UPM Serdang, Selangor, Malaysia

ARTICLE INFO

Keywords:
Carreau ternary hybrid nanofluid
Mhd
Heat generation
Nonlinear stretching sheet
Convective boundary conditions
Numerical solution

ABSTRACT

This study investigates the magnetohydrodynamic (MHD) mixed convection flow of a Carreau-based ternary hybrid nanofluid past a nonlinearly stretching surface with convective heating, internal heat generation, and radiative effects in a porous medium. The Carreau rheology accounts for shear-thinning behavior under varying Weissenberg numbers, while magnetic and radiation parameters model electromagnetic damping and thermal diffusion. The governing nonlinear partial differential equations are transformed via similarity variables and solved numerically using the Runge–Kutta–Fehlberg (RKF-45) method with a shooting technique. A comprehensive parametric study shows that increasing the Weissenberg number (We = 0–2) reduces the velocity by up to 16.8 %, whereas a higher magnetic parameter (M = 0–2) enhances thermal profiles by 12–15 % due to Joule heating. The radiation parameter (Rd = 0–1.2) elevates the wall temperature gradient, increasing the Nusselt number by 10.6 %, while the Biot number (Bi = 0.5–1.5) intensifies convective heat transfer by nearly 18 %. Conversely, increasing the viscosity index (n = 1.0–1.8) raises skin friction by 11 %, confirming the shear-thickening influence of the Carreau model.

1. Introduction

Ternary hybrid nanofluid (THNF) refers to a multiphase fluid system composed of a base fluid and a synergistic combination of three distinct types of nanoparticles, offering superior thermal and rheological characteristics compared to mono and binary nanofluids. These nanoparticles are specifically chosen to enhance certain thermophysical properties, such as thermal conductivity, viscosity, and stability, beyond what is achievable with single- or binary (two-particle) nanofluids. These fluids are extensively used in solar energy systems, electronic cooling, bioengineering, and thermal management in automotive and aerospace industries. Recent studies [1–3] have demonstrated the superior performance of ternary hybrid nanofluids in battery technologies, heat exchangers, and microchannel cooling systems. The performance of Li-ion batteries can be enhanced by the use of ternary hybrid nanofluids, as reported by Liu et al. [1]. Kumar et al. [2] analyzed two combinations of THNF: a) alumina + copper + multi-walled carbon nanotubes, and b) alumina + copper + graphene in a microchannel system. Additionally, Fahad et al. [3] investigated the thermal performance of a combination of alumina, carbon nanotubes, and graphene in helical heat exchangers.

* Corresponding author.
E-mail address: kiranbatool.60088@gmail.com (M. Karim).

https://doi.org/10.1016/j.rineng.2025.108085
Received 5 September 2025; Received in revised form 20 October 2025; Accepted 4 November 2025
Available online 5 November 2025

A Carreau fluid is a type of non-Newtonian fluid characterized by shear-thinning behavior at high shear rates and Newtonian characteristics at low shear rates [4,5]. The magnetohydrodynamics Carreau fluid has been reported [4–5], with analyses of simultaneous heat and mass transfer [4] and melting heat transfer [5]. However, when nanoparticles are dispersed in a Carreau fluid, it becomes a Carreau nanofluid. This type of nanofluid will have the same shear-thinning behavior as Carreau fluids, but enhanced thermal conductivity. Additionally, the formulation of Carreau nanofluid often combines the Carreau viscosity model with nanofluid heat transfer models (e.g., the Tiwari-Das or Buongiorno model). When ternary hybrid nanoparticles are suspended in a Carreau base fluid, the resulting Carreau ternary hybrid nanofluid exhibits complex rheological and thermal behavior. This model is applicable in polymer processing, biomedical flows, and enhanced oil recovery. The mathematical model, together with the numerical solutions for the Carreau nanofluid, has been described recently [6–7] for binary nanoparticles and [8–10] for ternary nanoparticles. Heat-mass transfer analysis is performed [6], whereas the fluid flow and heat transfer analysis is described [7] for the binary nanoparticles. The use of ternary nanoparticles in an engine oil nanofluid has been reported to enhance the overall aircraft performance efficiency [8]. On the other hand, the effects of ternary hybrid nanofluid in the biomedical field have been studied in the flow of permeable stenosed artery [9] and blood cells [10].

Magnetic fluids, also known as ferrofluids, are colloidal suspensions of magnetic nanoparticles (e.g., magnetite with a size below 10 nm) in a carrier liquid (e.g., oil or water). These fluids become magnetized in the presence of a magnetic field but are not necessarily electrically conductive. They can also become the controller in the heat and mass transfer, flow direction, and viscosity of the fluid flow. However, compared to magnetohydrodynamic fluid, the Lorentz force does not exist in magnetic fluid. Applications include micropowder technology [11], magnetic fluid hyperthermia [12], and biomedical delivery [13]. In heat transfer systems, magnetic fluids exhibit improved thermal regulation, as evidenced by numerical reports that have already proven this theory based on magnetic fluid flows over a moving plate [14], in twisted square tubes [15], and a cylinder [16]. Meanwhile, a magnetic nanofluid is a broader class of nanofluids that contains other nanoparticles, rather than magnetic nanoparticles (e.g., Cu, Ag, etc.). It is often designed not only for magnetism but also for enhanced heat transfer properties. Therefore, recent studies on magnetic nanofluids can be found in the following reports: [17–20]. The thermal performance of magnetite nanofluid has been described by Azizian [17]. The characteristics of magnetic nanofluid have been described due to the aspects of heat-mass transport for three different classifications of magnetic nanofluid: ferrite-based, metal-based, and iron-nitride-based [18]. Meanwhile, the usage of magnetic nanofluid over a curved minichannel and direct absorption solar collectors has been studied by Rahmoune and Bougoul [19] and Ma et al. [20].

A stretching sheet is a flat surface (horizontal or projected by a certain angle) that is being stretched continuously in its own plane. As the sheet stretches, it drags the adjacent fluid along, initiating a boundary layer flow over the sheet. The mathematical formulation for this type of boundary layer flow involves the Navier-Stokes equation. The related applications include polymer extrusion, coating, and fiber spinning, among others. Therefore, the recent studies of the boundary layer flow bounded by a stretching sheet have been reported in various aspects, such as in Newtonian fluid [21–22], Carreau fluid and Carreau nanofluid [4,6,23], nanofluid with binary nanoparticles [24,25], and nanofluid with ternary nanoparticles [26–28]. The following effects are being included in the mentioned models: Soret-Dufour effects [24] and Joule heating and slip condition [25]. Li et al. [26] incorporated the Cattaneo-Christov heat flux model to study the water-based ternary hybrid nanofluid. Besides, the ternary Casson nanofluid and the ternary blood-based hybrid nanofluid have been reported by Saleem et al. [27] and Manjunatha et al. [28], respectively.

Magnetite nanoparticles are nano-sized particles of iron oxide ($Fe3O4$) that exhibit the following properties: superparamagnetic at the nanoscale, <20 nm, high thermal conductivity, semiconducting, good biocompatibility, and often coated because magnetite is prone to oxidation. Copper oxide nanoparticles (CuO) are semiconducting metal oxide nanomaterials which own the following properties: high thermal conductivity, act as antibacterial and antifungal activity (useful in biomedical and environmental applications), have photocatalytic properties (used in solar cells, water splitting, and dye degradation), and are stable and chemically robust (widely used in various matrices). Molybdenum disulfide nanoparticles ($MoS2$) are nanostructures made from $MoS2$, a transition metal dichalcogenide (TMD) with a layered structure similar to graphite. $MoS2$ nanoparticles show enhanced thermal conductivity, lubrication, and anti-wear properties. Meanwhile, sodium alginate is a natural polysaccharide extracted from brown seaweed (algae) and is commonly used to create biocompatible, non-Newtonian fluids. When mixed with nanoparticles, it forms viscous solutions or gels with unique rheological and functional properties. Therefore, the studies related to the $Fe3O4$ [29,30], CuO [31,32], and $MoS2$ [33,34] nanoparticles have been reported, due to these effects: magnetic field [29], radiative heat flux [30], mixed convection [31], thermal radiation [32,34], second-order slip [33], and Joule heating [34]. On the other hand, sodium alginate nanofluid has been described recently by Faridi et al. [35], Jalil et al. [36], and Lone et al. [37]. The effect of magnetic induction has been considered by Faridi et al. [35] in their study of the flow of sodium alginate nanofluid. Jalil et al. [36] studied the sodium alginate ternary hybrid nanofluid between two parallel surfaces in a two-dimensional model. In contrast, Lone et al. [37] analyzed the sodium alginate ternary hybrid nanofluid over a stretching sheet in a three-dimensional model.

Viscous dissipation refers to the conversion of mechanical energy into thermal energy due to fluid viscosity during flow. In high-speed or high-viscosity flows, this effect can significantly influence temperature profiles and heat transfer rates. In problems involving heat transfer, viscous dissipation increases the fluid temperature, especially near walls, thickens the thermal boundary layer, and must be considered in the energy equation for accurate solutions. The interplay between viscous dissipation and ternary nanofluids has been modeled by Maheswari et al. [38], Matarneh et al. [39], Ramzan et al. [40], and Iqbal et al. [41], revealing significant temperature increases in confined flows and their role in determining the thermal boundary layer thickness. The various shapes have been chosen as a boundary for the ternary hybrid nanofluid, such as a flat sheet [37], cylinder [38], wedge [39], and curved surface [40].

Thermal radiation is the energy emitted by matter in the form of electromagnetic waves due to its temperature. In boundary layer flow over a surface, thermal radiation alters the temperature distribution, affects the heat transfer rate from or to the surface, and interacts with non-Newtonian fluid (especially in nanofluid). Thermal radiation becomes especially important when the surface temperature is very high, and the nanofluid participates in absorbing or emitting radiation. When coupled with ternary nanofluids, radiation effects have a significant influence on heat transfer in high-temperature environments, such as solar collectors and aerospace vehicles. Recent studies [41–44] have reported the impact of thermal radiation on boundary layer flow, confirming enhanced energy distribution and improved heat transport properties in ternary hybrid nanofluids. The additional factors considered in the radiated nanofluid system with ternary nanoparticles over a Riga plate [41], in the presence of gyrotactic microorganisms [42], include the Cattaneo-Christov heat flux model [44] and the Darcy-Forchheimer regime [44].

1.1. Motivation

Carreau-based ternary hybrid nanofluids are highly attractive for advanced cooling and processing applications such as polymer extru-

sion, electronics cooling, solar receivers, and biomedical perfusion, where fluids experience wide shear-rate ranges and high thermal loads. The Carreau rheology captures shear-thinning behavior, lowering viscosity under high shear for reduced drag while preserving low-shear pumpability. By combining CuO (high thermal conductivity), *Fe3O4* (magneto-responsiveness), and *MoS2* (lubrication and heat spreading), ternary suspensions achieve higher Nusselt numbers with manageable viscosity and controllable flow via magnetic fields, sustaining steep gradients under radiation, porous drag, and heat generation/absorption typical of high-flux devices.

1.2. Scientific gap

Most existing studies on magneto-thermal transport over stretching surfaces rely on Newtonian or at most binary nanofluid models, overlooking the dual impact of non-Newtonian rheology (e.g., Carreau shear-thinning and elastic effects) and multi-component nanoparticle interactions on heat transfer and drag. Rarely are these complexities treated alongside simultaneous MHD forcing, radiation, and heat generation/absorption within a unified similarity framework, leaving designers without reliable guidance for predicting ternary nanofluid performance in real-world, high-flux thermal systems.

1.3. Contribution

This work fills the gap above by developing and analyzing a Carreau-based ternary hybrid nanofluid model ($Fe3O4$, CuO, $MoS2$) embedded in sodium alginate over a nonlinear stretching sheet embedded in a porous medium, incorporating the effects of Weissenberg elasticity, magnetic fields, heat generation/absorption, radiation, and porosity. Unlike earlier Newtonian or binary formulations, the present study provides a comprehensive picture of coupled rheology and multi-nanoparticle tuning, offering practical insights into velocity, temperature, skin friction, and Nusselt behavior relevant to cooling technologies, energy devices, and industrial thermal management systems.

1.4. Model limitations

- The present formulation is based on a single-phase mixture model for the ternary hybrid nanofluid. Interphase slip, Brownian motion, thermophoresis, agglomeration, and sedimentation effects are neglected for simplicity.
- Radiative heat transfer is modeled using the Rosseland diffusion approximation with a lumped radiation parameter. Spectral dependence, temperature-dependent emissivity, and nonuniform absorption are not considered.
- The internal heat generation/absorption term is treated as a uniform volumetric source, neglecting spatial variations that may occur in practical systems.
- The applied magnetic field is assumed to be transverse and uniform, with a negligible induced field (low magnetic Reynolds number). Hall current, ion-slip, and electrochemical effects are excluded.
- The porous medium is considered homogeneous and isotropic with a single Darcy resistance parameter. Inertial, anisotropic, and temperature-dependent permeability effects are not modeled.
- The analysis assumes a steady, two-dimensional, laminar boundary-layer flow over a nonlinearly stretching surface. Three-dimensional, transient, or turbulent effects are outside the current scope.
- Thermophysical properties such as viscosity, density, and conductivity are treated as constant and state-independent, evaluated using algebraic mixture relations. Temperature- or shear-dependent property variations are neglected.
- A uniform convective boundary condition is applied at the wall. Possible variations in the surface heat transfer coefficient due to fouling, fluid property gradients, or surface roughness are ignored.

2. Mathematical formulation

We considered a Carreau nanofluid generated due to nonlinear stretching at the surface. The stretching velocity $u_w(x) = cx^m$ is assumed to vary nonlinearly from the origin, as illustrated in Fig. 1. Also, a magnetic field has strength B_0 and direction perpendicular to the sheet is pertained. Temperature and concentration in present flow are characterized by T_w and C_w respectively.

The rheological governing expressions for the steady flow of Carreau hybrid nanofluid are described as (see refs [5,7] and [23])

$$\frac{\partial u}{\partial x}+\frac{\partial v}{\partial y}=0, \tag{1}$$

$$u\frac{\partial u}{\partial x}+v\frac{\partial u}{\partial y}=\frac{\mu_{thnf}}{\rho_{thnf}}\frac{\partial^2 u}{\partial y^2}\left[1+\Gamma^2\left(\frac{\partial u}{\partial y}\right)^2\right]^{\frac{n-1}{2}} + \frac{\mu_{thnf}}{\rho_{thnf}}(n-1)\Gamma^2\frac{\partial^2 u}{\partial y^2}\left(\frac{\partial u}{\partial y}\right)^2\left[1+\Gamma^2\left(\frac{\partial u}{\partial y}\right)^2\right]^{\frac{n-3}{2}} - \left(\frac{\sigma_{thnf}}{\rho_{thnf}}B^2+\frac{\mu_{thnf}}{\rho_{thnf}}\frac{1}{k^*}\right)u \tag{2}$$

In above equations, Γ is the relaxation time of the Carreau fluid, k^* is the permeability of porous medium.

$$u\frac{\partial T}{\partial x}+v\frac{\partial T}{\partial y}=\left(\frac{k_{thnf}}{(\rho c_p)_{thnf}}+\frac{16\sigma^* T_\infty^3}{3(\rho c_p)_{thnf}k_f}\right)\frac{\partial^2 T}{\partial y^2}+\frac{Q_0}{(\rho c_p)_{thnf}}(T-T_\infty), \tag{3}$$

We consider steady, 2-D boundary-layer flow over a nonlinearly stretching sheet with a transverse magnetic field B_0 (no induced field, low magnetic Reynolds number). The wall velocity is $U_w(x) = ax^m$.The far field is quiescent. The radiative heat flux $q_r$is modeled using the Rosseland approximation, $q_r = -\frac{4\sigma^*}{3k^*}\frac{\partial T^4}{\partial y}$. To linearize the fourth-power temperature dependence, $T^4$is expanded about T_∞, yielding $T^4 \approx 4T_\infty^3 T - 3T_\infty^4$. Substitution gives $q_r = -\frac{16\sigma^* T_\infty^3}{3k^*}\frac{\partial T}{\partial y}$, which converts the radiation term into a linear temperature gradient form. Consequently, the energy equation includes an additional term proportional to the radiation parameter. $R_d = \frac{16\sigma^* T_\infty^3}{3k^* k}$, representing the enhancement of effective thermal diffusivity due to radiation.

The justified boundary conditions for the current analysis are

$$\left.\begin{array}{c} u=u_w(x), v=0, -k_{thnf}\dfrac{\partial T}{\partial y}=h_f(T_f-T), \text{ at y} = 0, \\ u\to 0, T\to T_\infty, \text{ as y}\to\infty. \end{array}\right\} \tag{4}$$

The porous resistance and a uniform heat source/sink enter the momentum and energy equations, respectively; the magnetic field acts normal to the sheet. The base fluid obeys the Carreau law (shear-thinning with a Newtonian plateau), parameterized via the Weissenberg number in the similarity ODEs; effective properties for the ternary suspension follow a single-phase (Tiwari–Das–type) model $\rho C_p, k_{eff}, \mu_{eff}$.

Targeted applications (polymer processing, microchannels, porous media cooling) operate across wide shear-rate ranges. Carreau rheology captures the observed shear-thinning at high shear with a Newtonian limit at low shear, which your Introduction already notes; the model also lets you probe elasticity via *We*and regime differences for $n < 1$vs $n > 1$that you report later in results. State that Newtonian and binary-nanofluid models miss these rheology-dependent thermal/drag trade-offs.

The thermophysical features of the Carreu-ternary hybrid nano liquid are delineated as:

$$\frac{\mu_{thnf}}{\mu_{bf}}=[(1-\varphi_1)(1-\varphi_2)(1-\varphi_3)]^{-2.5},$$

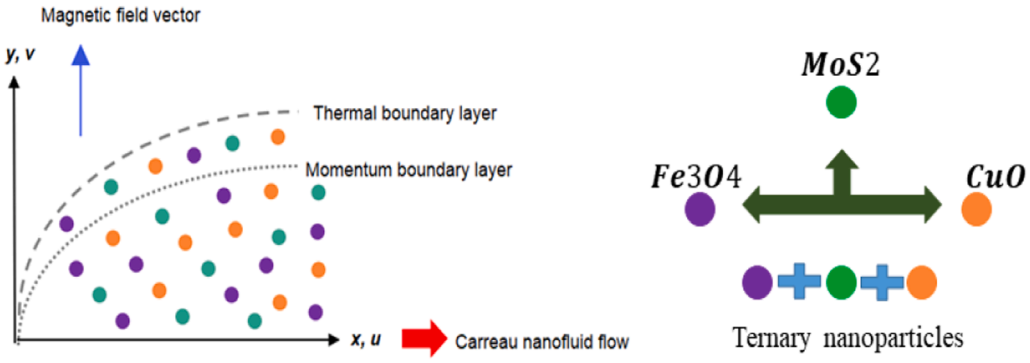

Fig. 1. Graphical illustration of the ternary hybrid Carreau nanofluid.

$$\frac{\rho_{hnf}}{\rho_{bf}} = (1-\varphi_1)\left[(1-\varphi_2)\left\{(1-\varphi_3)+\frac{\varphi_3\rho_3}{\rho_{bf}}\right\}+\frac{\varphi_2\rho_2}{\rho_{bf}}\right]+\frac{\varphi_1\rho_1}{\rho_{bf}},$$

$$\frac{(\rho c_p)_{thnf}}{(\rho c_p)_{bf}} = (1-\varphi_1)\left[(1-\varphi_2)\left\{(1-\varphi_3)+\frac{\varphi_3(\rho c_p)_3}{(\rho c_p)_{bf}}\right\}+\frac{\varphi_2(\rho c_p)_2}{(\rho c_p)_{bf}}\right] + \frac{\varphi_1(\rho c_p)_1}{(\rho c_p)_{bf}},$$

$$\frac{\sigma_{thnf}}{\sigma_{hnf}} = \left[\frac{\sigma_1(1+2\varphi_1)-\varphi_{hnf}(1-2\varphi_1)}{\sigma_1(1-\varphi_1)+\sigma_{hnf}(1+\varphi_1)}\right],$$

$$\frac{\sigma_{hnf}}{\sigma_{nf}} = \left[\frac{\sigma_2(1+2\varphi_2)-\varphi_{nf}(1-2\varphi_2)}{\sigma_2(1-\varphi_2)+\sigma_{nf}(1+\varphi_2)}\right],$$

$$\frac{\sigma_{nf}}{\sigma_{bf}} = \left[\frac{\sigma_3(1+2\varphi_3)-\varphi_{bf}(1-2\varphi_3)}{\sigma_3(1-\varphi_3)+\sigma_{bf}(1+\varphi_3)}\right],$$

$$\frac{k_{thnf}}{k_{hnf}} = \left[\frac{k_1+2k_{hnf}-2\varphi_1(k_{hnf}-k_1)}{k_1+2k_{hnf}+\varphi_1(k_{hnf}-k_1)}\right],$$

$$\frac{k_{hnf}}{k_{bf}} = \left[\frac{k_2+2k_{nf}-2\varphi_2(k_{nf}-k_2)}{k_2+2k_{nf}+\varphi_2(k_{nf}-k_2)}\right],$$

$$\frac{k_{nf}}{k_{bf}} = \left[\frac{k_3+2k_{bf}-2\varphi_3(k_{bf}-k_3)}{k_3+2k_{bf}+\varphi_3(k_{bf}-k_3)}\right],$$

In the above expression, φ_1, φ_2 and φ_3 reveal the solid nanoparticles' volume fraction of the MoS_2, CuO and Fe_3O_4 nanoparticles. Where the subscripts *thnf*, *hnf*, *nf*, *bf*, 1*s*, 2*s*, and 3*s* denote the ternary hybrid nanofluid, hybrid nanofluid, nanofluid base fluid, and the three distinct solid nanoparticles, respectively. Also, the physical properties data of these base fluids and hybrid nanoparticles are given in Table 1

Sodium alginate is a versatile substance with various applications in food, medicine, and cosmetics. It is commonly used as a thickener, stabilizer, and gelling agent in food products like ice cream, yogurt, and sauces. In pharmaceuticals, it's used in wound dressings and as a gelling agent in some medications. It also plays a role in textile printing and microencapsulation.

3. Method of solution

To simplify the flow governing equations and associated boundary conditions, introduce the following similarity transformations.

$$\psi = \sqrt{\frac{2c\nu_{bf}}{m+1}}x^{\frac{m+1}{2}}, \eta = \sqrt{\frac{(m+1)c}{2\nu_{bf}}}x^{\frac{m-1}{2}}y, \theta(\eta) = \frac{T-T_\infty}{T_f-T_\infty}. \tag{5}$$

It is evident that the similarity variables described in Eq. (5) satisfy Eq. (1) in exactly the same way. Now, one can obtain this by applying Eq. (5) to Eqs. (2–4);

$$\left\{1+nWe^2(f'')^2\right\}\left\{1+We^2(f'')^2\right\}^{\frac{n-3}{2}}f''' + \frac{A_2}{A_1}ff'' - \frac{A_2}{A_1}\left(\frac{2m}{m+1}\right)f'^2 - \left(\frac{2}{m+1}\right)\left(\frac{A_3}{A_1}M+K\right)f' = 0, \tag{6}$$

$$\left[A_5+\frac{4}{3}R_d\right]\theta'' + \mathrm{Pr}A_6f\theta' + \left(\frac{2}{m+1}\right)Pr\varepsilon\theta = 0, \tag{7}$$

The transformed boundary conditions are

$$f(0)=0, f'(0)=1, \theta'(0) = -\left(\sqrt{\frac{2}{m+1}}\right)\frac{1}{A_5}Bi(1-\theta(0)), f'(\infty)\to 0, \theta(\infty)\to 0. \tag{8}$$

Where, A_{1-6} symbolize the ratios of the thermophysical characteristics of Carreau HNF to those of the base fluid and are defined as

Table 1
Thermo-physical properties of nanoparticles and base fluid.

Properties	Notation	Units	Nanoparticles			Base fluid
			Fe3O4	*MoS2*	*CuO*	*SA*
Density	ρ	(kg/m^3)	5180	5060	6320	989
Specific heat	c_p	(J/kgK)	670	397.746	531.8	4175
Thermal conductivity	k	(W/mK)	9.7	34.5	76.5	0.6376
Electrical conductivity	σ	(S/m)	2.5×10^{-4}	2.09×10^{-4}	6.9×10^{-2}	2.6×10^{-4}

$$A_1=\frac{\mu_{thnf}}{\mu_{bf}}, A_2=\frac{\rho_{thnf}}{\rho_{bf}}, A_3=\frac{\sigma_{nf}}{\sigma_{bf}}, A_4=\frac{\sigma_{thnf}}{\sigma_{nf}}, A_5=\frac{k_{thnf}}{k_{bf}}, A_6=\frac{(\rho c_p)_{thnf}}{(\rho c_p)_{bf}}.$$

The parameters appear in Eqs. (6–8) the Weissenberg number $We=\sqrt{\frac{\Gamma^2 c^3 x^3}{\nu_{bf} x}}$, magnetic parameter $M=\frac{\sigma_{bf}B_0^2}{c\rho_{bf}}$, porosity parameter $K=\frac{\nu_{bf}}{ck^*}$, Radiation parameter $R_d=\frac{4\sigma^* T_\infty{}^3}{3k_1^* k_{bf}}$, Prandtl number $Pr=\frac{\nu_{bf}}{\alpha_{bf}}$, heat generation/absorption parameter $\varepsilon=\frac{Q_0}{c(\rho c_p)_{bf}}$.

Skin friction coefficient C_{fx}, the local Nusselt number Nu_x, are defined as

$$C_{fx}=\frac{\tau_w}{\rho_{bf}u_w^2}, Nu_x=\frac{xq_w}{k_{bf}(T_w-T_\infty)}. \tag{9}$$

The surface shear stress τ_w, surface heat flow q_w, wall mass flux q_s are determined by,

$$\tau_w=\mu_{thnf}\frac{\partial u}{\partial y}\left[1+\Gamma^2\left(\frac{\partial u}{\partial y}\right)^2\right]_{y=0}^{\frac{n-1}{2}}, q_w=-k_{thnf}\left[\frac{\partial T}{\partial y}\right]_{y=0}. \tag{10}$$

Employing the similarity transformation (8), we can write

$$\begin{cases}(Re_x)^{\frac{1}{2}}Cf_x=\sqrt{\frac{m+1}{2}}A_1 f''(0)\left[1+We^2(f''(0))^2\right]^{\frac{n-1}{2}}\\ (Re_x)^{-1/2}Nu_x=-\sqrt{\frac{m+1}{2}}\left[1+\frac{4}{3}R_d\right]A_5\theta'(0).\end{cases} \tag{11}$$

Where $Re_x=\frac{cx^{m+1}}{\nu_{bf}}$ is the local Reynolds number.

4. Numerical methodology

The similarity equations are solved with assumed boundary conditions via a shooting method with adaptive Runge–Kutta–Fehlberg (RKF45) for the IVP and a Newton update on the unknown wall slopes. RKF45 provides embedded error control and automatic step selection, which is well-suited for boundary-layer ODEs whose stiffness intensifies at large η. To guard against shooting ill-conditioning, we (i) scale state variables, (ii) use secant damping on the wall-slope iterates, and (iii) enforce a far-field tolerance $|y(\eta_{max})-\mathbf{y}_\infty|<10^{-8}$ with $\eta_{max}=10--14$ (extended if needed). We independently cross-check with a collocation BVP solver (finite-difference/collocation with tridiagonal Newton) to ensure that wall metrics $C_f\propto f''(0)$and $Nu\propto-\theta'(0)$are mesh-independent.

4.1. Grid convergence and validation of numerical scheme

Grid convergence was assessed using three similarity grids with a constant refinement ratio r. For each wall quantity, the observed order $p$was obtained from the three solutions (ϕ_3,ϕ_2,ϕ_1), and the Richardson extrapolated value $\phi_{ext}$was computed. The fine-grid GCI quantified numerical uncertainty, GCI_{12}. Across all cases, GCI_{12} for $f''(0)$and $-\theta'(0)$remained below 2 %, and the asymptotic-range indicator was consistent with r^p, confirming grid-independent results. Domain-truncation tests with increased η_{max} produced no material changes in wall metrics, further validating convergence.

4.2. Verification (code & discretization)

- Absolute/relative IVP tolerances: 10^{-8}; maximum step doubling/halving per stage: 2; Jacobian banding in the BVP solver.
- Domain truncation study: increase η_{max}until wall metrics change $<10^{-5}$.
- Grid/step convergence: compute three grids (coarse/medium/fine) and report GCI for $f''(0)$and $-\theta'(0)$; target GCI ≤ 2 %.
- Energy balance check: monitor integral heat flux vs. wall source/sink term to confirm residuals $<10^{-8}$.

4.3. Validation (physics & literature consistency)

1. Newtonian limit: set $n=1$and $We=0$ in the Carreau model; with $M=0$, $\varepsilon=0$, radiation off, and $\phi_i=0$, recover the classical stretching-sheet boundary layer; compare $f''(0)$and $-\theta'(0)$ against published Newtonian benchmarks (tabulate 3–5 points).
2. Single/binary nanoparticle reduction: hold total $\phi=\phi_1+\phi_2+\phi_3$fixed and set two $\phi_i=0$; verify that trends of Nu with ϕ match reported mono/binary behaviors (conductivity gain vs. viscosity penalty).

5. Results and discussion

This study analyzes the thermal and flow behavior of Carreau ternary hybrid nanofluids containing 3 % $3O4$, CuO, and $MoS2$ nanoparticles in sodium alginate. It highlights key differences between pseudoplastic and dilatant fluids under varying Weissenberg numbers and magnetic fields. At We = 0, the fluid behaves as a Newtonian fluid, while increasing We introduces viscoelastic effects, with We = 2 exhibiting strong elastic dominance and flow asymmetry. Velocity decreases with increasing We, especially in dilatant fluids, and magnetic fields further suppress flow. The ternary nanoparticles enhance thermal conductivity and increase the Nusselt number, thereby improving heat transfer during heat generation or absorption. These results are essential for designing efficient thermal systems in engineering and biomedical applications. The numerical simulations regarding dimensionless velocity, temperature, skin friction, and Nusselt numbers are presented graphically. To validate the current study, the results as a limiting case are compared with previously published results in the literature and presented in Table 2.

In Fig. 2(a), the dimensionless velocity f'(η) is shown for pseudoplastic ternary nanofluids. As the Weissenberg number We increases (from 0 to 2), the velocity profiles exhibit a noticeable reduction. This is because a higher We represents more substantial elastic effects due to fluid memory, which resists flow and slows down the velocity within the boundary layer. The pseudoplastic nature (shear-thinning) further amplifies this effect, where the viscosity decreases with increased shear rate, reducing momentum transfer near the wall and compressing the boundary layer. Regarding the magnetic field, when $M=0$ (blue lines), the velocity is significantly higher compared to $M=1$ (green dashed lines). An increasing magnetic parameter introduces a Lorentz force that opposes the motion of the electrically conducting nanofluid, thereby reducing its velocity. This magnetic damping effect is more evident near the wall and causes a sharper decay of velocity with respect to the similarity variable η.

Fig. 2(b) illustrates the behavior of dilatant (shear-thickening) ternary nanofluids. Similar to the pseudoplastic case, increasing the Weissenberg number results in a consistent decline in the velocity profiles. The elastic resistance arising from higher We restricts the rate of deformation, thus decreasing the velocity throughout the boundary layer. However, due to the shear-thickening property of the dilatant

Table 2
Comparison of $-\theta(0)$ for Pr and m for viscous fluid when $M=K=R_d=0$, $Bi\to\infty$.

m	Cortell [45]		Zaimi et al. [46]	
	Pr = 1	Pr = 5	Pr = 1	Pr = 5
0.2	0.610262	1.607175	0.61131	1.60757
0.5	0.395277	1.586744	0.59668	1.58658
1.5	0.574537	1.557463	0.57686	1.55751
2.0	-	-	0.57245	1.55093
3.0	0.564472	1.542337	0.56719	1.54271
4.0	-	-	0.56415	-
10.0	0.554960	1.528573	0.55783	1.52877

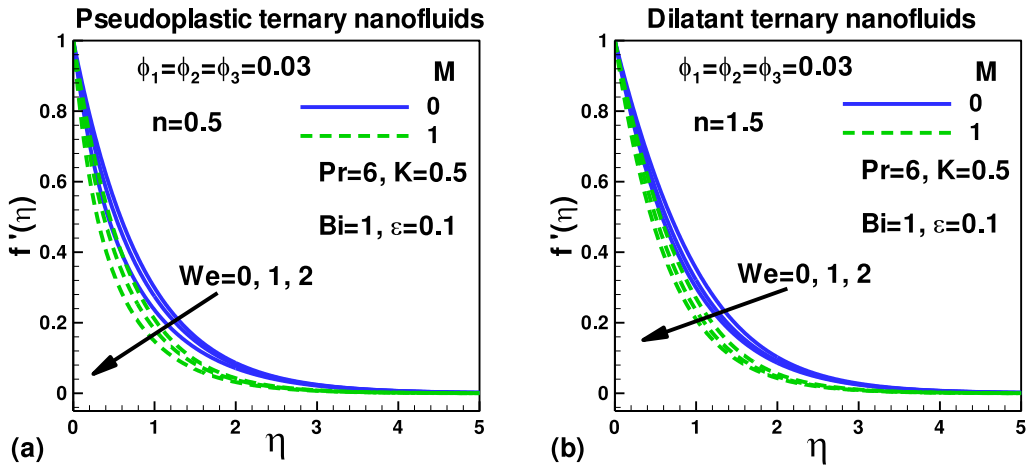

Fig. 2. Impact of Magnetic Field (M) and Weissenberg Number (We) on Dimensionless Velocity Profiles.

fluid, the effective viscosity increases with shear, leading to an even more restricted flow and relatively thinner boundary layers compared to pseudoplastic fluids. When comparing magnetic field effects, the velocity again diminishes for $M = 1$ versus $M = 0$, reinforcing the suppressive influence of the Lorentz force. The dilatant fluid's higher resistance to deformation makes it more sensitive to magnetic field effects, contributing to a sharper decline in velocity near the surface.

Comparing Figs 2(a) and 2(b), it is evident that the pseudoplastic fluid exhibits a thicker boundary layer than the dilatant one. In pseudoplastic fluids, the decreasing viscosity at higher shear rates facilitates momentum diffusion deeper into the fluid, leading to a more extended boundary layer. Conversely, dilatant fluids, with their increasing viscosity under shear, inhibit this diffusion and compress the boundary layer. Both increasing We and M contribute to suppressing the velocity in the boundary layer. Still, their combined effect is more pronounced in the dilatant case due to the additive resistance from shear-thickening behavior.

Fig. 3(a) demonstrates how the dimensionless velocity f′(η) of pseudoplastic ternary nanofluids responds to variations in the stretching parameter mm (from 0 to 2) and porous medium resistance K. As m increases—representing a transition from no stretching ($m = 0$) to linear ($m = 1$) and then nonlinear stretching ($m = 2$)—the velocity profiles decrease, indicating a thinner boundary layer. This behavior is due to the enhanced strain in the fluid near the wall as stretching increases, which suppresses the upward transport of momentum and thus reduces the velocity across the boundary layer. In the absence of porosity ($K = 0$), the difference between velocity profiles for different m values is modest because the fluid can flow relatively freely. However, when $K = 1$, representing a porous medium, the resistance to flow increases significantly. In this case, the impact of increasing mm becomes more pronounced: the stretching-induced thinning of the boundary layer is now amplified by the porous drag, leading to a stronger reduction in velocity. The porosity parameter K introduces a Darcy-like resistive force that opposes the flow. This resistance reduces the fluid's ability to maintain high velocities away from the wall, thereby compressing the velocity boundary layer. Hence, a higher K results in a thinner boundary layer and a more rapid decay of velocity with respect to η. In Fig. 3(b), similar trends are observed, but the suppression in velocity due to both stretching and porosity is more severe. As the stretching parameter mm increases, the velocity profiles systematically decline, indicating a more substantial shear influence at the wall. This effect is especially significant for dilatant fluids, which exhibit increasing viscosity with shear rate. Thus, the nonlinear stretching leads to higher shear-induced viscosity, further resisting the flow and causing more pronounced velocity attenuation. Again, when $K = 0$, the velocity differences across different m values are minimal. However, for $K = 1$, the porous drag intensifies the impact of stretching. The flow within a porous medium is subject to internal resistance, and in shear-thickening fluids, this resistance is compounded by the fluid's increasing viscosity. As a result, both nonlinear stretching and porosity work synergistically to reduce

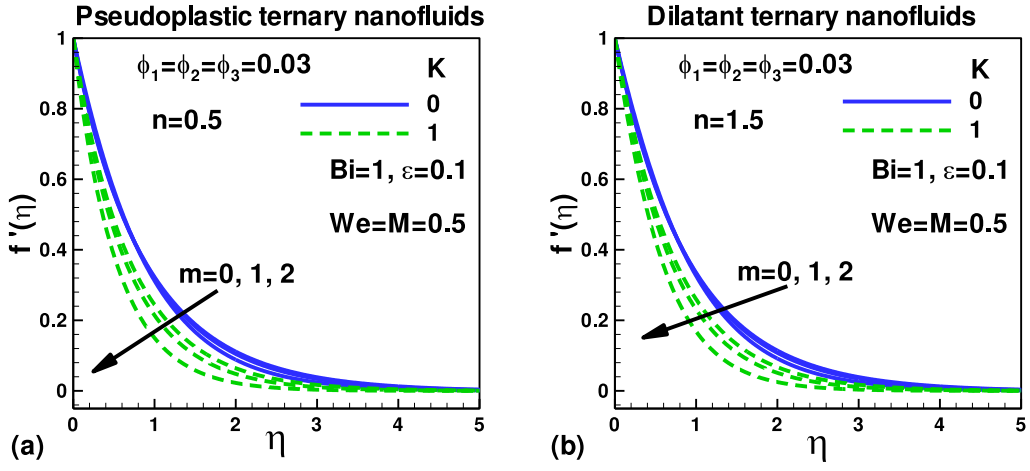

Fig. 3. Impact of Stretching Parameter (m) and Porosity Parameter (K) on dimensionless Velocity Profiles.

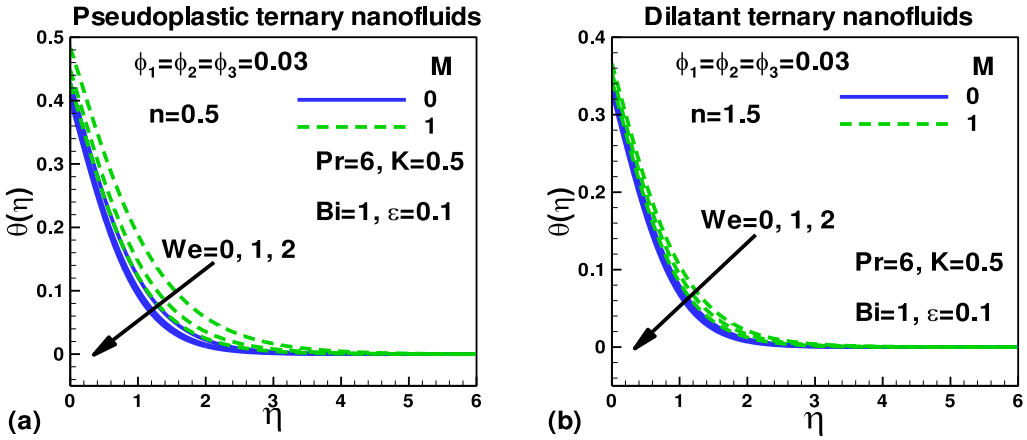

Fig. 4. Impact of magnetic field and Weissenberg Number on dimensionless temperature profiles.

momentum transfer and compress the boundary layer. Compared to pseudoplastic fluids, dilatant fluids exhibit stronger suppression in the presence of stretching and porosity due to their shear-thickening behavior.

In Fig. 4(a), the dimensionless temperature θ(η) for pseudoplastic Carreau-ternary nanofluids is shown as a function of the similarity variable η, under the influence of varying Weissenberg number We and magnetic field parameter M. As We increase from 0 to 2, the temperature profile decreases significantly throughout the thermal boundary layer. This occurs because a higher Weissenberg number reflects stronger fluid elasticity, which resists deformation and flow. This elastic resistance reduces viscous heating and suppresses heat generation, resulting in a decrease in surface temperature and a more uniform thermal energy distribution within the boundary layer. For the magnetic field effect, when $M = 0$ (solid lines), the temperature is lower compared to the case with $M = 1$ (dashed lines). The presence of a magnetic field introduces a Lorentz force, which acts against fluid motion, producing internal friction and thus generating additional heat (Joule heating). This increases the fluid temperature and consequently enhances the thermal boundary layer thickness. Therefore, the temperature profiles show a slower decay for $M = 1$, reflecting a thicker thermal layer due to heat accumulation.

In the case of dilatant nanofluids, (Fig. 4(b), similar trends are observed. Increasing the Weissenberg number leads to a decline in both the surface temperature and the thermal boundary layer. As the fluid becomes more elastic, heat conduction is diminished due to suppressed velocity gradients and limited internal energy transfer. This causes a more rapid drop in temperature away from the surface, indicating a thinner thermal boundary layer with higher We. When the magnetic field is introduced ($M = 1$), the dimensionless temperature increases across the boundary layer compared to the $M = 0$ case. The magnetic field-induced damping slows the fluid, reducing convective heat transfer but increasing localized heating due to electromagnetic effects. This explains the expansion of the thermal boundary layer as the magnetic field strength increases.

When comparing Figs. 4(a) and 4(b), it is evident that dilatant fluids exhibit lower surface temperatures and thinner thermal boundary layers compared to pseudoplastic fluids. This can be attributed to the shear-thickening behavior of dilatant fluids, which increases their effective viscosity under shear. Higher viscosity resists motion and reduces thermal diffusion away from the wall, resulting in more rapid temperature decay and a compressed thermal profile. In contrast, pseudoplastic fluids (shear-thinning) exhibit reduced viscosity under shear, promoting both flow and thermal dispersion, thereby forming a thicker thermal boundary layer.

In Fig. 5(a), the dimensionless temperature θ(η) for pseudoplastic Carreau-ternary nanofluids is plotted for varying values of the radiation parameter Rd=0, 1, 2 and Biot number Bi=0.5, 1. It is observed that as Rd increases, the surface temperature and the temperature within the thermal boundary layer rise. This is because higher thermal radiation enhances radiative heat transfer from the surface into the fluid, effectively increasing the thermal energy available in the boundary layer and raising the local temperature. Consequently, the thermal boundary layer

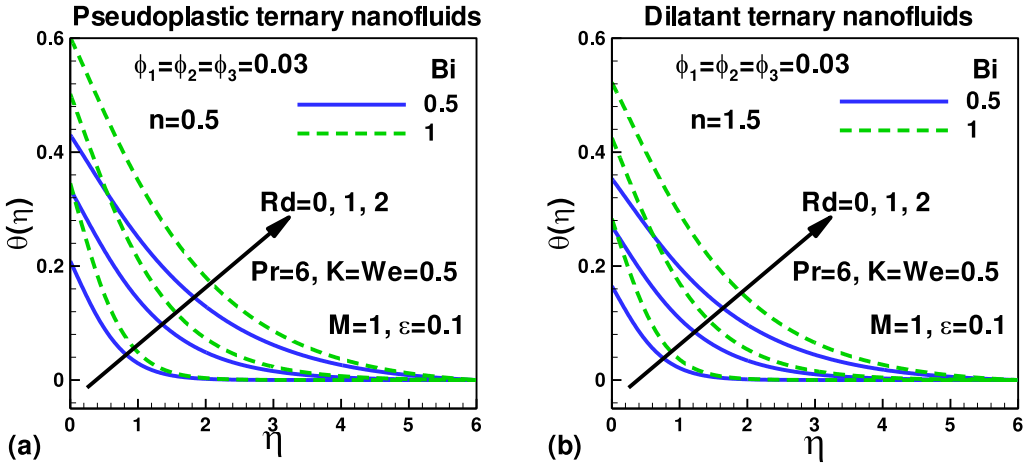

Fig. 5. Influence of radiation parameter (Rd) and Biot number (Bi) on dimensionless temperature profiles.

becomes thicker due to the increased thermal diffusion. Similarly, increasing the Biot number—which characterizes the ratio of convective to conductive heat transfer at the surface—leads to higher dimensionless temperatures. A larger Bi value implies more effective heat transfer from the surface to the fluid, thus increasing the surface temperature and allowing heat to penetrate deeper into the fluid. This results in an expanded thermal boundary layer.

For the dilatant ternary nanofluids (Fig. 5b), a similar trend is observed. As the radiation parameter Rd increases, the dimensionless temperature profiles shift upward. This is because the radiation contributes an additional heat source, enhancing energy transport through the fluid. As a result, the thermal boundary layer thickens due to elevated temperatures and the accumulation of heat within the boundary layer. An increase in Biot number likewise elevates the temperature profiles. Higher Bi values indicate improved convective heat transfer at the boundary, which promotes a higher surface temperature and deeper thermal diffusion into the fluid. This widens the thermal boundary layer and raises the temperature field. However, the extent of temperature elevation and boundary layer thickening is less in dilatant fluids compared to pseudoplastic ones. This is attributed to the shear-thickening nature of dilatant fluids, which increases viscosity with shear rate, thereby resisting heat and momentum diffusion more strongly. As a result, heat transfer remains more localized near the wall, even in the presence of radiation and enhanced surface convection. When comparing Figs. 5(a) and 5(b), pseudoplastic nanofluids exhibit higher surface temperatures and thicker thermal boundary layers than their dilatant counterparts. This difference arises due to the lower effective viscosity in pseudoplastic fluids under shear, which promotes more efficient heat transport through the fluid. In contrast, dilatant fluids resist flow and diffusion due to increasing viscosity with shear, leading to more restricted thermal development. Thus, under the influence of both radiation and higher Biot numbers, the thermal response is more pronounced in pseudoplastic nanofluids, making them better suited for applications requiring enhanced heat dissipation.

Negative skin friction refers to a scenario where the wall shear stress (or drag) acts in the opposite direction of the fluid flow due to complex surface-fluid interactions, such as reversed flow or strong stretching effects. It typically implies opposing the imposed flow direction, and its control is vital in applications such as drag reduction, enhanced surface cooling, and microfluidic device optimization. Fig. 6(a) shows the variation of scaled negative skin friction with the stretching parameter m, for different values of magnetic field M and Weissenberg number We. As mm increases (representing enhanced stretching), negative skin friction increases. This occurs because stronger stretching leads to larger velocity gradients at the wall, thereby improving the magnitude of shear stress. For a fixed Weissenberg number, increasing the magnetic field intensifies the negative skin friction. This is due to the Lorentz force, which resists the motion of electrically conducting fluids and enhances velocity gradients near the wall, increasing the magnitude of opposing (negative) skin friction. At We=0, the fluid behaves like a Newtonian fluid. Pseudoplastic nanofluids, with their shear-thinning nature, generate higher velocity gradients near the wall under stretching, resulting in greater negative skin friction. This effect is accentuated under low-elasticity conditions (low We). However, for We = 1, the pseudoplastic behavior is overridden by elastic memory effects, which resist shear and reduce wall stress. Thus, at higher We, the negative skin friction is lower compared to dilatant fluids.

In Fig. 6(b), the dilatant nanofluids exhibit overall higher negative skin friction with increasing stretching m, similar to the pseudoplastic case. However, the response to Weissenberg's number is notably different. At We=0, the dilatant fluids exhibit lower negative skin friction compared to pseudoplastic fluids. This is because the shear-thickening behavior increases the fluid's resistance to deformation, lowering the shear rate at the wall under Newtonian-like conditions. Conversely, at We=1, elastic effects become significant. For dilatant fluids, the combination of elastic resistance and shear-thickening leads to an amplified wall shear under non-Newtonian conditions, resulting in a greater rise in negative skin friction compared to pseudoplastic fluids. Moreover, the magnetic field continues to raise negative skin friction by adding resistive drag and intensifying the boundary-layer shear, as seen from the upward trend in all dashed (higher M) curves. The comparison between pseudoplastic and dilatant Carreau-ternary nanofluids reveals that pseudoplastic fluids exhibit higher negative skin friction under Newtonian conditions (We=0) due to their shear-thinning nature, which enhances near-wall velocity gradients during stretching. In contrast, dilatant fluids show greater negative skin friction at higher Weissenberg numbers (We=1), where elastic and shear-thickening effects compound to intensify wall shear stress. Overall, dilatant nanofluids demonstrate stronger resistance to flow under non-Newtonian conditions, resulting in larger negative skin friction values. These findings have significant engineering implications: in microfluidic and biomedical devices, controlling skin friction is essential for optimizing flow resistance and shear-sensitive processes; in thermal management systems, elevated wall shear enhances convective cooling; and in coating, extrusion, and polymer processing, tuning skin friction via stretching or magnetic fields allows precise control over fluid behavior near surfaces for better product quality and energy efficiency. In Fig. 7(a), the variation of negative skin friction is presented for pseudoplastic ternary hybrid nanofluids under

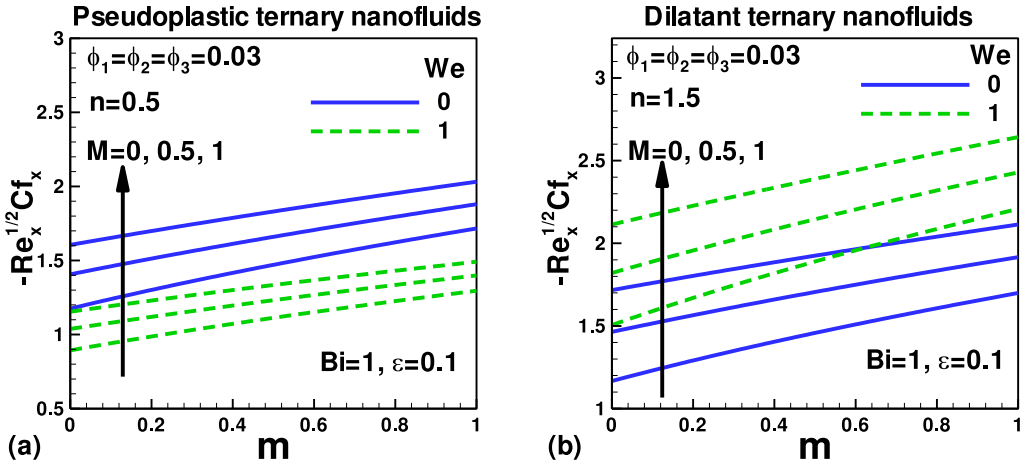

Fig. 6. Variation of negative skin friction with stretching parameter for different values of magnetic field and Weissenberg number in Carreau-ternary hybrid nanofluids.

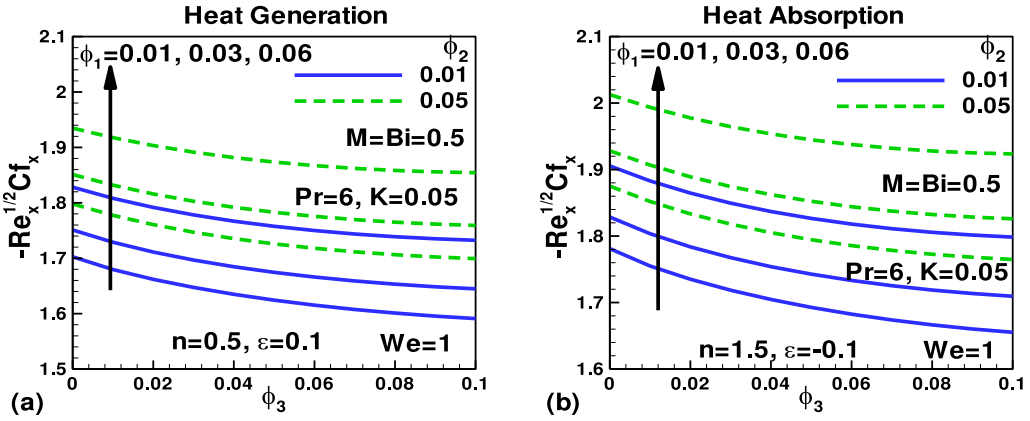

Fig. 7. Variation of negative skin friction with volume fraction of selected nanoparticles in Carreau-ternary hybrid nanofluids.

heat generation conditions (ε=0.1). As the volume fraction of CuO nanoparticles (ϕ_3) increases from 0 to 0.1, the negative skin friction decreases. This behavior is attributed to the high density and thermal conductivity of CuO, which increase the fluid's effective viscosity and thermal capacity, thereby reducing wall shear by suppressing velocity gradients near the surface. Conversely, increasing the volume fractions of *Fe3O4* (ϕ_1) and *MoS2* (ϕ_2) leads to an increase in negative skin friction. Fe_3O_4 has strong magnetic and moderate thermal properties, while *MoS2* offers excellent lubrication characteristics and moderate density. Both particles enhance momentum diffusion and amplify near-wall shear stress, particularly in non-Newtonian fluids such as pseudoplastics, thereby increasing skin friction.

For dilatant nanofluids undergoing heat absorption (ε=−0.1), a similar trend is observed (Fig. 7b). The addition of CuO nanoparticles reduces negative skin friction as ϕ_3 increases. This again results from CuO's contribution to increased viscosity, which is more pronounced in shear-thickening (dilatant) fluids, further restricting near-wall motion and lowering wall shear. In contrast, both *Fe3O4* and *MoS2* nanoparticles enhance negative skin friction as their volume fractions increase. *Fe3O4* contributes to stronger magnetic interactions and internal friction, while *MoS2*'s excellent tribological properties improve shear transfer at the wall. These effects counteract the thermal absorption and induce stronger surface drag. The comparison reveals that negative skin friction is higher under heat absorption than heat generation in both fluid types. This is because heat absorption cools the fluid, reducing temperature-dependent viscosity weakening and thus maintaining higher viscosity near the wall. This results in steeper velocity gradients and stronger surface shear. In contrast, heat generation warms the fluid, softening viscosity and reducing skin friction. Hence, thermal absorption leads to enhanced wall shear and higher negative skin friction compared to thermal generation conditions.

Fig,8(a) illustrates the effect of the power-law index *n* and nanoparticle volume fractions (ϕ_1, ϕ_2) on negative skin friction in Carreau-ternary hybrid nanofluids under heat generation (ε=0.1). As *n* increases from 0.5 to 1.5, the fluid transitions from pseudoplastic (shear-thinning) to dilatant (shear-thickening) behavior. An increase in *n* results in greater resistance to deformation, which enhances velocity gradients near the wall and leads to the rise in negative skin friction. Furthermore, increasing the volume fractions of *Fe3O4* (ϕ_1) and *MoS2* (ϕ_2) nanoparticles results in an additional increase in skin friction. These nanoparticles improve thermal and momentum diffusivity due to their favorable thermophysical properties, which intensify the shear stress near the wall. However, the rise is more moderate in heat generation scenarios, as elevated temperatures soften viscosity and slightly offset the increase in wall drag. Fig. 8(b) displays the same behavior under heat absorption conditions (ε=−0.1). The trend of increasing skin friction with the power-law index *n* is again observed. Dilatant nanofluids (higher n) generate more negative skin friction due to their higher apparent viscosity under shear, which leads to stronger velocity gradients and higher wall shear. The effect of nanoparticle volume fractions (ϕ_1 and ϕ_2) is more pronounced under heat absorption. As the fluid absorbs heat, it cools, leading to an increase in viscosity, which magnifies the influence of *Fe3O4* and *MoS2* on the boundary layer shear. Consequently, skin friction increases more sharply in comparison to the

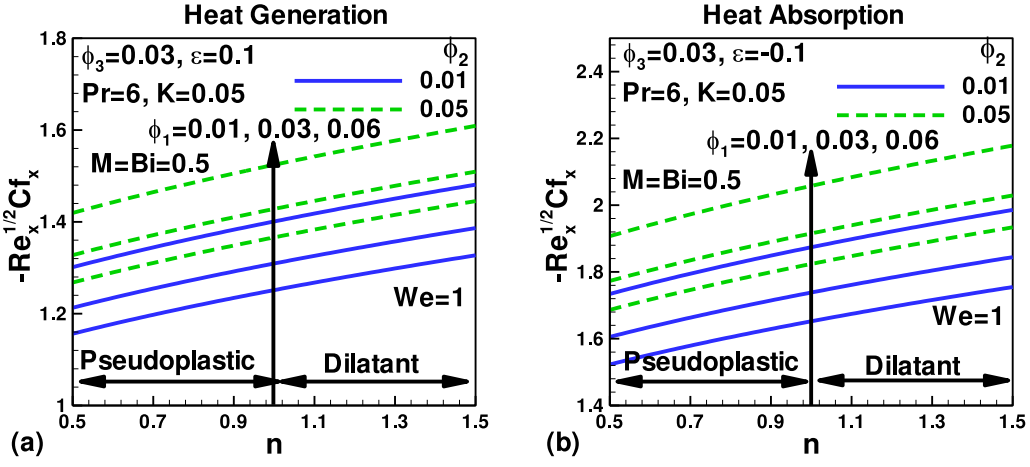

Fig. 8. Variation of negative skin friction with power-law index and volume fraction of selected nanoparticles in Carreau-ternary hybrid nanofluids.

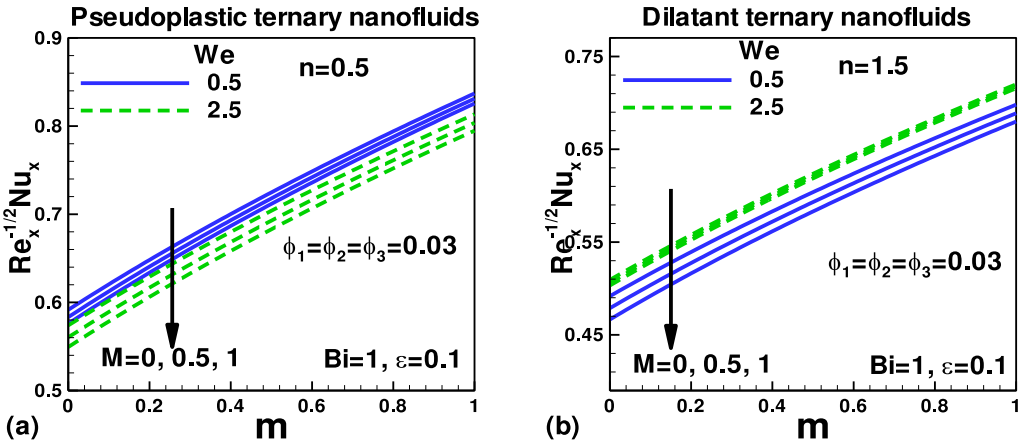

Fig. 9. Variation of Nusselt number with stretching parameter for various values of magnetic field and Weissenberg number in Carreau-ternary hybrid nanofluids.

heat generation case. Across both cases, negative skin friction is consistently higher in the heat absorption case. This occurs because heat absorption reduces thermal energy, increasing viscosity and making the fluid more resistant to flow.

This resistance steepens the velocity gradient near the surface and enhances wall shear stress. In contrast, heat generation raises fluid temperature and reduces viscosity, leading to lower shear at the wall and reduced skin friction. Thus, heat absorption enhances the skin frictional effects of both fluid rheology and nanoparticle loading. Fig. 9 (a) illustrates the variation of the local Nusselt number as a function of the stretching parameter m, for different values of the Weissenberg number (We = 0.5 and 2.5) and magnetic field strength (M = 0, 0.5, 1), with a fixed Biot number (Bi = 1), heat generation parameter ε=0.1, and equal nanoparticle volume fractions ($\phi_1=\phi_2=\phi_3$=0.03). These results correspond to pseudoplastic Carreau ternary hybrid nanofluids (power-law index n = 0.5). In the absence of a magnetic field (M = 0), the Nusselt number is highest. As the magnetic field strength increases, the Nusselt number decreases. This is because the Lorentz force induced by the magnetic field acts as a resistive body force, which retards fluid motion and thereby reduces convective heat transfer, ultimately decreasing the surface heat transfer rate (Nusselt number).

Additionally, an increase in the Weissenberg number (We)—a parameter that characterizes the fluid's elasticity—lowers the Nusselt number for pseudoplastic fluids. This is because larger We values enhance the fluid's relaxation time, leading to more pronounced elastic effects that suppress thermal boundary layer thinning, thereby reducing the heat transfer rate. This behavior is particularly relevant in polymer extrusion, plastic sheet cooling, and thermal regulation in flexible electronics, where pseudoplastic nanofluids are used to maintain desired surface temperatures under stretching conditions. Engineers must exercise caution when dealing with magnetic field intensities and viscoelastic properties in such systems to optimize heat transfer performance.

Fig. 9(b) examines the Nusselt number variation for dilatant Carreau ternary hybrid nanofluids with a power-law index n = 1.5, under similar parametric conditions as in Fig. 9(a). Here, the Nusselt number also increases with the stretching parameter mm, but the overall values are lower compared to those of pseudoplastic fluids. However, in contrast to Fig. 9(a), the Nusselt number increases with increasing Weissenberg number (We = 0.5 to 2.5). This reversal in trend arises because dilatant fluids exhibit increased resistance with shear rate. When elasticity (captured by We) is present, it assists in stabilizing the momentum and thermal boundary layers. The additional elastic stress in dilatant fluids can enhance energy storage and release mechanisms, leading to more effective energy transfer from the surface to the fluid, thereby resulting in a higher Nusselt number. The magnetic field still induces a damping effect, reducing the Nusselt number. However, the suppression is milder due to the inherently higher resistance of dilatant fluids to deformation, which already limits convective motions. This behavior is significant in viscous mineral processing, abrasive slurry flows, and materials such as paints and dough, where dilatant behavior predominates. Controlling elasticity via We and minimizing adverse magnetic effects can improve thermal regulation in such applications.

Comparing both subfigures, pseudoplastic nanofluids yield a higher Nusselt number than dilatant nanofluids under identical conditions. This is primarily due to the shear-thinning nature of pseudoplastic fluids (lower viscosity at higher shear rates), which facilitates faster boundary layer thinning and more effective convective heat transfer. Conversely, dilatant fluids (shear-thickening) resist deformation, making them thermally less responsive to the same stretching and viscoelastic conditions. This comparative analysis is critical in tailoring nanofluid types to suit specific thermal engineering needs: pseudoplastic fluids for applications requiring enhanced heat dissipation, and dilatant fluids for those where thermal stability and damping are prioritized.

Fig. 10(a) shows how the Nusselt number increases with the radiation parameter Rd for pseudoplastic ternary nanofluids (n = 0.5), under varying Biot number (Bi=0.2, 0.5, 0.8) and heat generation parameter ε=0.1 and 0.5. Other parameters are kept constant ($\phi_1=\phi_2=\phi_3$=0.03 M=We=1, Pr=6, K = 0.05). As the radiation parameter Rd increases, the Nusselt number consistently rises for all Biot numbers. This occurs because thermal radiation enhances the transport of thermal energy within the fluid. For pseudoplastic nanofluids, which thin under shear, the improved thermal energy due to radiation synergizes with increased convective activity, boosting the heat transfer rate. The Biot number reflects the ratio of internal to external thermal resistance. A higher Bi indicates stronger convective heat exchange at the boundary, which naturally increases the surface heat transfer, resulting in higher Nusselt numbers. When the heat generation parameter ε is high (0.5), the internal energy source raises the fluid temperature, which thickens the thermal boundary layer and reduces the temperature gradient at the surface. As a result, the Nusselt number decreases. Lower ε values support higher heat transfer rates. This thermal performance is significant in polymer cooling, thermal inkjet printing, and nanofluid-based surface coatings, where rapid heat removal is vital and pseudoplastic behavior is desired.

Fig. 10(b) presents the corresponding behavior for dilatant ternary nanofluids (n = 1.5), using the same parameter sets as in Fig. 10(a). The Nusselt number is plotted against the radiation parameter Rd, for different Biot numbers and two values of the heat generation parameter ε. Again, increasing the radiation parameter enhances the Nusselt number. Thermal radiation acts as an additional energy carrier, improving the thermal conductivity-like effect in the flow, which is especially beneficial in fluids that resist flow (shear-thickening). Even

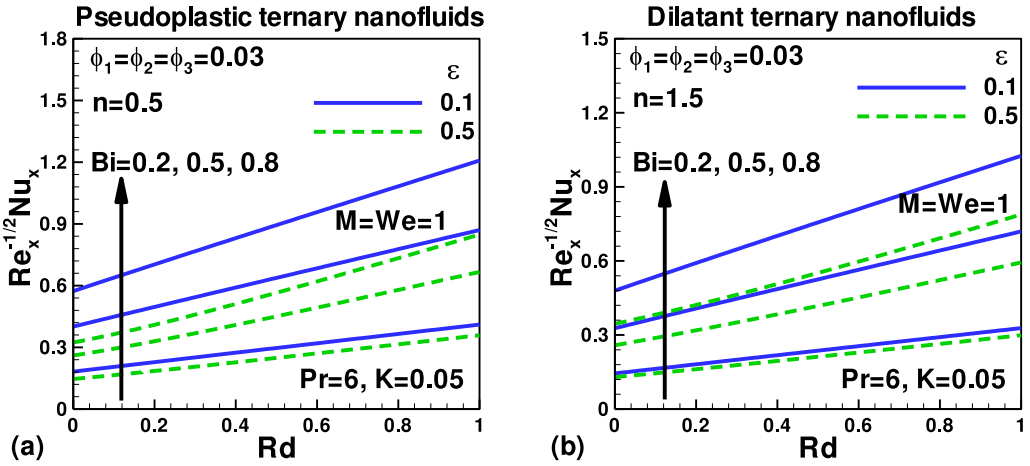

Fig. 10. Variation of Nusselt number with radiation parameter for various values of Biot number and heat generation parameter in Carreau-ternary hybrid nanofluids.

though dilatant fluids are more resistant to shear, the added radiative effect helps improve heat conduction, which is reflected in an upward trend in the Nusselt number. An increase in Biot number leads to more vigorous surface convection, again resulting in a higher surface heat transfer rate and increased Nusselt numbers. Higher heat generation rates ($\varepsilon = 0.5$) result in more energy being produced internally, thereby reducing the thermal gradient at the surface. This results in a lower Nusselt number due to the suppression of outward heat flux. In contrast, with less heat generation ($\varepsilon = 0.1$), the thermal boundary remains thinner, thereby enhancing the heat transfer rate. Such behavior is crucial in heat-resistant slurry flows, industrial coatings, and additive manufacturing applications, where dilatant fluids are utilized for their robust mechanical response but may lag in thermal responsiveness.

Across both cases, the pseudoplastic nanofluids demonstrate consistently higher Nusselt numbers than dilatant nanofluids under similar conditions, particularly in the presence of heat generation. The shear-thinning behavior of pseudoplastic fluids enables easier flow and thinner thermal boundary layers, thereby facilitating greater heat transfer. In contrast, shear thickening in dilatant fluids results in more viscous resistance, which hinders convective heat transfer, especially under strong heat generation, where internal energy accumulation suppresses thermal gradients. This comparison highlights the suitability of pseudoplastic ternary nanofluids in high-efficiency heat dissipation systems, such as microchannel cooling, thermal spreaders, and innovative coatings, where managing internal heat generation is critical.

Fig. 11(a) presents the variation of the local Nusselt number with the power-law index ***n*** for different nanoparticle volume fractions $\phi_1$and ϕ_2 in a Carreau-based ternary hybrid nanofluid subjected to heat generation (ε=0.1). Here, ϕ_3=0.03, and other parameters are fixed: Pr=6, K = 0.05, M=Bi=0.5, We=1. As the power-law index n increases from pseudoplastic ($n < 1$) to dilatant ($n > 1$) behavior, the Nusselt number decreases. This trend occurs because higher n implies increased shear-thickening resistance, which leads to thicker thermal boundary layers and reduced convective heat transfer efficiency. In contrast, pseudoplastic fluids thin under shear, facilitating the thinning of the boundary layer and enhancing surface heat transfer. Regarding nanoparticle volume fractions ϕ_1 and ϕ_2, their increase leads to higher Nusselt numbers. Nanoparticles such as metal oxides, CNTs, and graphene possess high thermal conductivities, so increasing their concentration enhances the overall thermal conductivity of the nanofluid, resulting in better heat conduction and higher convective heat transfer rates. This scenario is particularly applicable to electronic cooling and microreactor systems, where internal heat generation is significant and enhanced thermal performance is required without excessively increasing flow resistance.

Fig. 11(b) illustrates the variation of the local Nusselt number with the power-law index n and varying nanoparticle volume fractions under heat absorption conditions ($\varepsilon = -0.1$). All other parameters are identical to Fig. 11(a). Once again, increasing the number of nodes (n) results in a

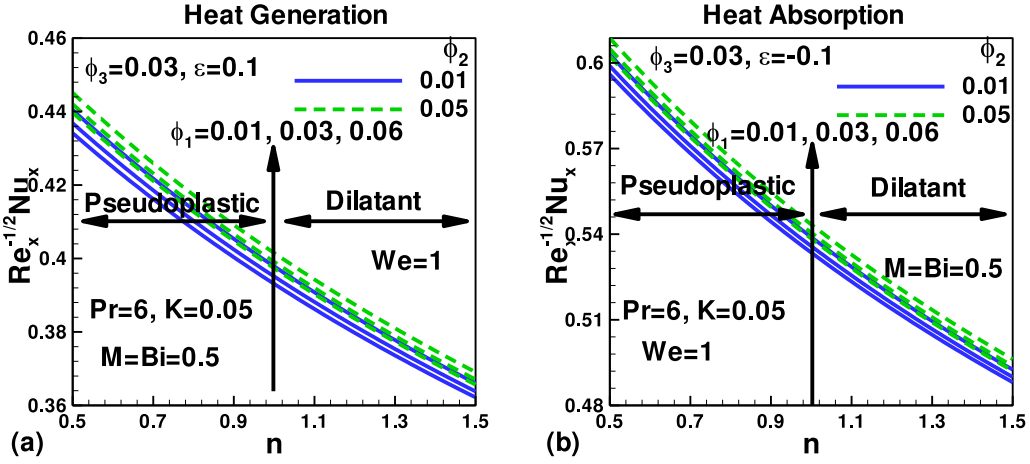

Fig. 11. Variation of Nusselt number with power-law index and volume fraction of selected nanoparticles in Carreau-ternary hybrid nanofluids.

decline in the Nusselt number, consistent with the transition from pseudoplastic to dilatant behavior. Dilatant fluids resist shear and suppress the flow-induced enhancement in heat transfer, while pseudoplastic fluids support better thermal transport due to their shear-thinning nature. Higher nanoparticle volume fractions ϕ_1 and ϕ_2 lead to an increase in the Nusselt number. The improved thermal conductivity provided by a higher concentration of nanoparticles results in a reduction in the thermal boundary layer thickness, thereby enhancing the rate of surface heat absorption. However, compared to the heat generation case, the Nusselt number is consistently higher in the heat absorption scenario. This is because the removal of internal heat enhances the thermal gradient between the wall and the fluid, thereby improving the convective heat transfer rate. Conversely, internal heat generation tends to diminish this gradient, reducing heat transfer efficiency. This behavior is essential for thermal energy storage systems, solar absorber design, and regenerative cooling, where heat absorption must be maximized, and fluid rheology and nanoparticle tuning can be strategically employed.

The comparison between Figs 11(a) and 11(b) reveals several key insights into the thermal behavior of Carreau-based ternary hybrid nanofluids under heat generation and heat absorption conditions. In both cases, the Nusselt number decreases with an increase in the power-law index n, indicating that pseudoplastic fluids (with lower n) offer superior heat transfer performance compared to dilatant fluids due to their shear-thinning nature, which promotes boundary layer thinning and enhances convective heat transfer. Additionally, increasing the volume fractions of nanoparticles ϕ_1 and ϕ_2 consistently improves the Nusselt number, as the effective thermal conductivity of the fluid rises with higher nanoparticle content, facilitating better thermal transport. Notably, the Nusselt number is higher in the heat absorption case than in the heat generation case. This is because heat absorption intensifies the thermal gradient between the wall and the fluid, leading to stronger convective heat transfer. In contrast, internal heat generation reduces this gradient and diminishes the rate of surface heat transfer.

Figs 12(a) and 12(b) explain the variation of the Nusselt number with the volume fraction of selected nanoparticles (ϕ_1, ϕ_2, and ϕ_3) in Carreau-ternary hybrid nanofluids during heat generation and heat absorption. In the heat generation scenario (Fig. 12a), the Nusselt number decreases with increasing ϕ_3 for all values of ϕ_1 and ϕ_2. The behavior suggests that the volume fraction of the third nanoparticle (ϕ_3) has a diminishing effect on heat transfer. This could be due to the influence of the third nanoparticle on the overall fluid's viscosity or its interaction with the heat conduction properties of the nanofluid, leading to reduced convective heat transfer as the volume fraction of the third nanoparticle, ϕ3, increases. As ϕ_1 and ϕ_2 increase, the Nusselt number rises because the presence of these nanoparticles enhances the fluid's thermal conductivity and its ability to transfer heat efficiently. The addition of nanoparticles, such as ϕ1 and ϕ2, improves heat conduction, resulting in enhanced heat transfer.

Similar to the heat generation case, the Nusselt number is higher at lower ϕ_3 values and decreases as ϕ_3 increases (Fig. 12b). However, there is a noticeable difference in the behavior for heat absorption. Here, the Nusselt number for heat absorption is lower than that for heat generation at the same values of ϕ_1 and ϕ_2. This could be due to different thermal dynamics in the absorption process, where the heat transfer rate depends not only on thermal conductivity but also on other factors, such as the nanoparticle's ability to absorb or release heat energy. Since the heat absorption process typically involves lower heat flux, the ability of the nanofluid to enhance convective heat transfer becomes relatively less significant, resulting in lower Nusselt numbers in comparison to heat generation. The higher Nusselt number observed in the heat generation case can be attributed to the stronger influence of nanoparticles on convective heat transfer during a heating process, where the heat flux is generally higher and the thermal gradients are steeper. In contrast, during heat absorption, the fluid may experience a more uniform temperature distribution, resulting in less enhancement of heat transfer efficiency. Thus, the Nusselt number remains lower during absorption. The present results are compared with the existing literature:

- **Ternary vs. mono/binary nanofluids.** The present findings, which indicate that ternary blends can outperform mono/binary cases (via higher effective conductivity at similar loadings), are consistent with reports of superior performance of ternary hybrids in batteries, heat exchangers, and microchannel systems. The introduction summarizes these outcomes and provides citations [1–3].
- **Carreau rheology (pseudoplastic vs. dilatant).** The observed decrease of Nu_x with increasing power-law index n(pseudoplastic >dilatant) aligns with Carreau-fluid expectations summarized in your text and with previous Carreau/Carreau-nanofluid studies you reference.
- **MHD (Lorentz braking).** Present results that more vigorous Msuppresses convection and lowers Nu_x concur with prior MHD analyses for Carreau and related non-Newtonian bases noted in your literature overview.
- **Thermal radiation and Biot number.** The trends observed in this study, with Rd and Bi (enhanced wall heat exchange and modified thermal layer), are in line with recent studies on radiation-coupled ternary hybrids over canonical surfaces (Riga plate, Darcy–Forchheimer, and CattaneoChristov) [42–45].

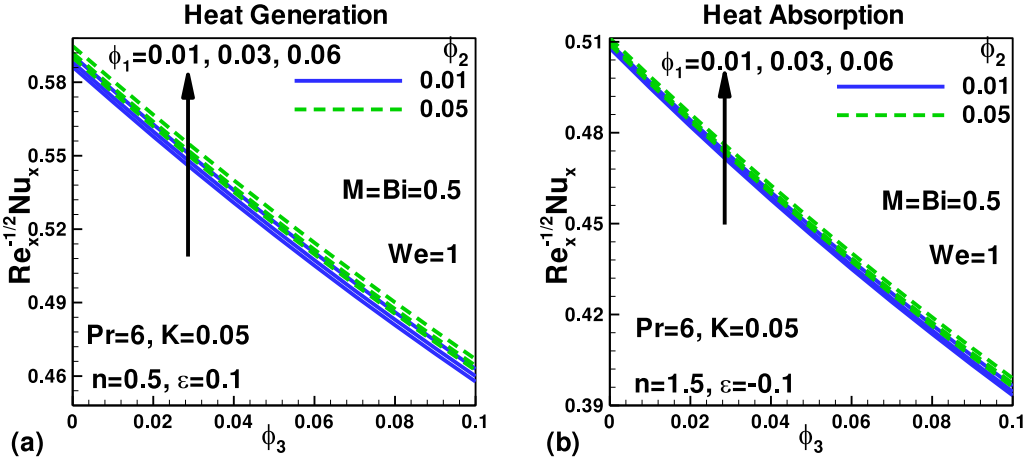

Fig. 12. Variation of Nusselt number with volume fraction of selected nanoparticles in Carreau-ternary hybrid nanofluids.

- **Internal heat source/sink.** Present results and discussion show that heat generation ($\varepsilon > 0$) reduces Nu_x and absorption ($\varepsilon < 0$) increases it—matching classical boundary-layer behavior and the narrative you provide for Figs. 10,11.
- **Nanoparticle-specific effects.** Nu_x increasing with ϕ_1, $\phi_2$but potentially decreasing with ϕ_3 when viscosity penalties dominate—mirror the conductivity–viscosity trade-off emphasized in your discussion of Fig. 12.
- **Scope matches the application literature.** Your application framing (polymer processing, microelectronics cooling, and porous heat-exchange media) is consistent with the use cases cataloged in the manuscript's related work survey.

Two concrete validation steps to add (strengthens credibility further)

1. **Newtonian limit check.** Set $n = 1$, $We = 0$, $\phi_i = 0$, $M = 0$, $\varepsilon = 0$, radiation off—recover the classical stretching-sheet baseline and tabulate $f''(0)$, $-\theta'(0)$ against published Newtonian benchmarks (3–5 points).
2. **Binary/mono reductions.** Hold total ϕ fixed and set two. $\phi_i = 0$; verify that $Nu_x(\phi)$ trends match the mono/binary cases cited in our review, confirming the ternary closures' consistency with known limits. (Report these in a small validation table.)

These comparisons, already foreshadowed by our literature review and figure narratives, will make the manuscript's results read as a natural, validated extension of prior Newtonian, MHD, radiation-coupled, and binary/ternary nanofluid studies—solidifying credibility.

Model limitations:

- **Single-phase (mixture) treatment.** Nanoparticles are modeled only through effective properties; interphase slip, Brownian/thermophoretic migration, agglomeration, and settling are neglected. This follows the Carreau-nanofluid + effective-property closure referenced in your Introduction; it improves tractability but omits micro-scale transport that can alter near-wall gradients at higher loadings.
- **Idealized radiation and volumetric heating.** Radiative effects are represented by a lumped radiation parameter *Rd*and internal heat generation/absorption by a uniform source term, which do not capture spectral radiation, temperature-dependent emissivities, or spatially varying heat release found in real devices. (Radiation and heat-source terms are part of your stated scope.)
- **MHD simplifications.** The analysis assumes a transverse magnetic field with a negligible induced field (low magnetic Reynolds number) and no Hall/ion-slip/electrochemical effects. The distinction between ferrofluid and true MHD, highlighted in your review, underscores that not all "magnetic fluids" support Lorentz forcing—our model presumes an electrically conducting suspension.
- **Porous medium idealization.** The porous layer is treated as homogeneous and isotropic with a single resistance parameter; pore-scale inertia/dispersion, anisotropy, and temperature-dependent permeability are not modeled. (Porous resistance is included at the formulation level but with lumped parameters.)
- **Boundary-layer and geometry assumptions.** Two-dimensional, steady, laminar boundary-layer flow over a nonlinearly stretching sheet is assumed; three-dimensionality, curvature, unsteadiness, surface roughness, and separation are outside the scope.
- **Thermophysical properties.** Effective conductivity, viscosity, and heat capacity are taken from algebraic mixture rules and treated as state-independent within each case; temperature- or shear-dependent nanoparticle properties and interfacial thermal resistance are not included. (Your text frames the use of ternary effective-property closures but not temperature dependence.)
- **Carreau rheology scope.** The Carreau law captures shear-thinning with a Newtonian plateau but not thixotropy, yield stress, or viscoelastic normal-stress differences beyond what is implicit in the Weissenberg-number scaling; extensional rheology effects are not resolved.
- **Thermal boundary condition.** A uniform convective boundary condition (constant h) is imposed; spatially varying interfacial heat transfer (e.g., due to fouling or nonuniform coolant) is not modeled.
- **Validation envelope.** The study currently lacks an experimental comparison; credibility rests on the consistency of trends and limiting-case arguments (Newtonian/MHD limits). Incorporating benchmarks would narrow uncertainty and calibrate model constants.

Implication. These assumptions are standard for first-principles similarity analyses, enabling a clear view of parameter influences (e.g., *M, We, Rd, ε, Bi*). However, they limit applicability to dilute, well-dispersed, laminar regimes with modest radiation complexity and homogeneous porous resistance. Future work can relax these restrictions by adding Buongiorno transport, temperature-dependent properties, anisotropic/Forchheimer porous models, higher-*Re*/3-D effects, and targeted experimental validation.

6. Conclusion

In conclusion, this study presents a comprehensive analysis of MHD flow of Carreau ternary hybrid nanofluids, considering both heat generation and absorption effects. The findings emphasize the role of nanoparticle composition, Weissenberg number, and magnetic fields in modulating the flow and heat transfer behavior. Pseudoplastic fluids show better heat transfer efficiency due to their shear-thinning nature, while dilatant fluids exhibit higher resistance to flow. The study's results can be applied to optimize heat dissipation in thermal management systems, indicating that fluid rheology and nanoparticle design are crucial to enhancing thermal performance in various industrial applications. The key findings are summarized below:

- Increasing the Weissenberg number results in reduced velocity profiles, with dilatant fluids showing a stronger suppression compared to pseudoplastic fluids.
- The magnetic field reduces fluid velocity, especially near the wall, with the effect being more significant in dilatant nanofluids.
- Pseudoplastic fluids exhibit thicker boundary layers compared to dilatant nanofluids.
- The Nusselt number decreases with higher Weissenberg number and the magnetic field strength, while it increases with higher nanoparticle volume fractions.
- CuO nanoparticles tend to reduce negative skin friction, while Fe_3O_4 and MoS_2 increase it due to their enhanced momentum diffusion properties.
- Heat generation results in lower Nusselt numbers, while heat absorption leads to higher values; dilatant fluids exhibit less heat transfer efficiency than pseudoplastic fluids.

6.1. Future extensions

Future work can explore the inclusion of more complex boundary conditions, such as variable permeability in the porous medium or unsteady flow, to further model real-world applications with greater accuracy. The effect of varying nanoparticle shapes and sizes on the fluid's thermal and flow characteristics should also be examined. Additionally, experimental validation of the numerical models presented in this study would provide more substantial evidence of the benefits of ternary hybrid nanofluids in enhancing heat transfer in MHD systems.

Nomenclature

Roman Letters	
B_0	Strength of magnetic field ($kgs^{-2}\,A^{-1}$)
Bi	Biot number
C_{f_x}	Skin friction coefficient
c_p	Specific heat of nanoparticles ($J/(K.kg)$)
h_f	Convective heat transfer ($W/m^2.K$)
h_s	Convective mass transfer
k^*	is the permeability of porous medium
K	Porosity parameter
k_{thnf}	Thermal conductivity of ternary-hybrid nanofluid
k_{bf}	Thermal conductivity of base fluid ($W/m.K$)
k_1^*	Mean absorption coefficient
M	Magnetic parameter
N_{u_x}	Local Nusselt number
P_r	Prandtl number
q_r	Radiative heat flux
q_w	Wall heat flux
R_d	Radiation parameter
Re_x	Local Reynold number
T	Fluid Temperature
T_f	Convective Fluid temperature
T_∞	Fluid ambient temperature
$u,\ v$	Velocity components (m/s)
u_w	Stretching sheet velocity(m/s)
W_e	Weissenberg number
x, y	Coordinate axis
Greek letters	
η	Similarity variable
ε	heat generation/absorption parameter
Γ	relaxation time
μ_{bf}	Dynamic viscosity of base fluid (kg/ms^3)
μ_{thnf}	Dynamic viscosity of ternary-hybrid nanofluid
ν_{bf}	Kinematic viscosity of base fluid (m^2/s)
ρ_{thnf}	Density of ternary-hybrid nanofluid
ρ_{bf}	Density of base fluid (kg/m^3)
ρ_p	Density of nanoparticles
ϕ	Dimensionless nanoparticle concentration
ψ	Stream function
σ_{bf}	Electrical conductivity of base fluid
σ_{thnf}	Electrical conductivity ternary-hybrid nanofluid
σ^*	Stefan-Boltzmann constant
τ_w	Wall shear stress
θ	Dimensionless temperature
Subscripts	
∞	Condition at free stream
w	Condition at wall

Conflict of interest

None.

CRediT authorship contribution statement

Imran Ullah: Investigation. **Waqar A. Khan:** Methodology. **Maimoona Karim:** Writing – original draft. **Syed M. Hussain:** Software. **Hijaz Ahmad:** Validation. **Wasim Jamshed:** Visualization, Supervision. **Siti Suzilliana Putri Mohamed Isa:** Resources, Project administration, Funding acquisition, Data curation.

Declaration of competing interest

The authors declare that they have no known competing financial interests or personal relationships that could have appeared to influence the work reported in this paper.

Data availability

Data will be made available on request.

References

[1] Q. Liu, F. Liu, S. Liu, Y. Wang, S. Panchal, M. Fowler, R. Fraser, J. Yuan, J. Zhao, Improved performance of Li-ion battery thermal management system by ternary hybrid nanofluid, J. Energy Storage 109 (2025) 115234.

[2] K. Kumar, J. Sarkar, S.S. Mondal, Analysis of ternary hybrid nanofluid in microchannel-cooled cylindrical Li-ion battery pack using multiscale multi-domain framework, Appl. Energy 355 (2024) 122241.

[3] M.K. Fahad, M.J. Hasan, N.F. Ifraj, D.C. Dey, Numerical investigation on the impact of different design arrangements of helical heat exchangers with varying cross-sections utilizing ternary hybrid nanofluids, Heliyon. 10 (14) (2024).

[4] S.S.P.M. Isa, H.M. Azmi, N. Balakrishnan, N.M. Arifin, H. Rosali, N.S. Ismail, Heat and mass transfers in the boundary layer flow of mixed convection magnetohydrodynamic non-Newtonian Carreau fluid, Magnetohydrodynamics 60 (no. 3–4) (2024) 181–196.

[5] R. Khan, S. Zeb, Z. Ullah, M. Yousaf, I. Samuilik, Carreau fluid flow analysis with inclined magnetic field and melting heat transfer, Partial. Differ. Equ. Appl. Math. 13 (2025) 101030.

[6] S.S.P.M. Isa, A.N.M. Som, N. Balakrishnan, Heat/mass transfer performance in magnetohydrodynamic Carreau hybrid nanofluid with dual nanoparticles (molybdenum disulfide and silica), Magnetohydrodynamics 60 (no. 3–4) (2024) 285–301.

[7] K. Bhaskar, K. Sharma, K. Bhaskar, Heat interaction and slip-induced flow in Carreau hybrid nanofluid dynamics, J. Therm. Anal. Calorim. (2025) 1–17.

[8] J. Iqbal, F.M. Abbasi, Advanced cooling and solar aircraft applications using MHD Carreau trihybrid nanofluid with solar radiation, Int. J. Mod. Phys. B (2025) 2550210.

[9] Y. Akhtar, S. Ahmad, F. Khalid, M. Junjua, Y. Aryanfar, A.H.S. Hendy, M. Abd El-Rahman, S.M. Hussain, Spectral relaxation method to investigate novel ternary hybrid Carreau nanofluid model with permeable stenosed artery, ZAMM-J. Appl. Math. Mech./Zeitschrift für Angewandte Mathematik und Mechanik 105 (no. 1) (2025) e202400491.

[10] A. Riaz, M. Naeem Aslam, M. Ali Awan, M.W. Aslam, S. Ullah Khan, S. Akram, E. E. Mahmoud, Peristaltic flow of electromagnetic tri-hybrid Carreau nanofluid using backpropagated Levenberg–Marquardt technique: an entropy generation analysis in blood cells, Electromagn. Biol. Med. 44 (no. 2) (2025) 193–211.

[11] M. Szczęch, W. Horak, Research on magnetic fluid seals using fluids produced by grinding micropowder technology, Tribologia (2025).

[12] H. Patel, K. Parekh, Hyperthermic response optimization for Mn0. 5Zn0. 5Fe2O4 magnetic fluid for its application in magnetic fluid hyperthermia, J. Magn. Magn. Mater. 615 (2025) 172777.

[13] Y. Yu, C. Zhang, X. Yang, L. Sun, F. Bian, Microfluidic synthesis of magnetic nanoparticles for biomedical applications, Small. Methods 9 (no. 4) (2025) 2401220.

[14] A. Kamran, E. Azhar, S.M. Atif, Magnetic dipole interactions with tangent hyperbolic ferromagnetic fluid over a moving plate: a numerical study, Numer. Heat Transf. B: Fundam. 86 (no. 4) (2025) 981–997.

[15] J. Jongpluempiti, P. Vengsungnle, S. Poojeera, N. Naphon, S. Eiamsa-ard, P. Naphon, Analysis of heat transfer and flow behaviors of magnetic fluid in twisted square tubes with alternating electromagnetic fields, Eng. Sci. 34 (2025) 1432.

[16] A. Bhandari, Impact of a magnetic dipole on heat transfer in non-conducting magnetic fluid flow over a stretching cylinder, Fluid Dyn. Mater. Process. 20 (no. 3) (2024).

[17] R. Azizian, A fundamental study on heat transfer characteristics of magnetite nanofluids, PhD diss. Open Res. Newctle. (2025).

[18] F. Xu, Y. Cao, H. Gong, J. Li, Y. Xu, L. Shi, Mass transport and energy conversion of magnetic nanofluids from nanoparticles' Movement and liquid manipulation, Processes 12 (no. 5) (2024) 955.

[19] I. Rahmoune, S. Bougoul, Effect of magnetic field and magnetic nanofluid on heat transmission improvement in a curved minichannel: I. Rahmoune, S. Bougoul, J. Therm. Anal. Calorim. 149 (no. 2) (2024) 729–744.

[20] M. Ma, S. Qing, X. Zhang, M. Hu, Z. Jia, Heat transfer performance study of magnetic Fe2O3/graphene nanofluid in DASC, Int. J. Thermophys. 46 (no. 5) (2025) 68.

[21] A.K. Pandey, K. Bhattacharyya, A.K. Gautam, S. Rajput, M.S. Mandal, A. J. Chamkha, D. Yadav, Insight into the relationship between nonlinear mixed convection and thermal radiation: the case of newtonian fluid flow due to nonlinear stretching, Propuls. Power Res. 12 (no. 1) (2023) 153–165.

[22] S.S.P.M. Isa, A. Hazirah Mohd, B. Nanthini, N. Aina Suhaiza Mohamad, A. Kartini, I. Nurul Syuhada, M.A. Norihan, R. Haliza, The Soret-Dufour effects on three-dimensional magnetohydrodynamics newtonian fluid flow over an inclined plane, CFD Lett. 16 (no. 9) (2024) 39–51.

[23] T. Akaje, O.M.A. Yusuff, B.I. Olajuwon, M.T. Raji, Impact of nonlinear thermal radiation on MHD stagnation-point flow of Carreau nanofluid over a stretching plate with homogeneous and heterogeneous chemical reactions, Heat. Transf. Res. 56 (no. 15) (2025).

[24] S.S.P.M. Isa, S. Parvin, N. Arifin, F. Ali, K. Ahmad, Soret-Dufour effects on the water-based hybrid nanofluid flow with nanoparticles of Alumina and Copper, Malays. J. Math. Sci. 17 (no. 3) (2023) 283–304.

[25] T. Abbas, Magnetohydrodynamic flow of a hybrid nanofluid over an exponentially stretching sheet with joule heating and slip conditions using spectral collocation method with legendre wavelets, Multiscale Multidiscip. Model Exp. Des. 8 (no. 1) (2025) 125.

[26] W. Li, S. Ali Khan, M. Shafqat, Q. Abbas, T. Muhammad, M. Imran, Computational analysis for efficient thermal transportation of ternary hybrid nanofluid flow across

a stretching sheet with Cattaneo-Christov heat flux model, Case Stud. Therm. Eng. 66 (2025) 105706.
[27] M. Saleem, A. Al-Zubaidi, N. Radwan, S. Saleem, H. Adawi, Thermal effects of ternary Casson nanofluid flow over a stretching sheet: an investigation of Thomson and Troian velocity slip, Case Stud. Therm. Eng. 65 (2025) 105561.
[28] S. Manjunatha, V. Puneeth, A. Kuttan Baby, C.S. Vishalakshi, Examination of thermal and velocity slip effects on the flow of blood suspended with aluminum alloys over a bi-directional stretching sheet: the ternary nanofluid model, Waves Random Complex Media 35 (no. 2) (2025) 3961–3978.
[29] P.E.S. Mustafa, S.M. Zokri, N.S. Arifin, S.F.H.M. Kanafiah, A.R.M. Kasim, H.A. M. Al-Sharifi, Numerical investigation of Non-Newtonian Williamson hybrid ferrofluid flow over a stretching sheet: effects of magnetic, stretching and thermal parameters, Semarak. Int. J. Fundam. Appl. Math. 5 (no. 1) (2025) 25–34.
[30] U. Yashkun, L. Ali Lund, K. Zaimi, Z. Shah, M.A.H. Alshehri, N. Vrinceanu, E. Antonescu, Computational study of magnetite-ethylene glycol–water-based hybrid nanofluid dynamics on an exponential shrinking/stretching Riga surface under radiative heat flux, Colloid. Polym. Sci. 303 (no. 1) (2025) 95–109.
[31] S. Jahan, M. Ferdows, E. Tzirtzilakis, Convective flow of hybrid nano particles in combination of TiO2+ CuO/engine oil MoS2+ ZnO/engine oil, and Al2O3+ Cu/engine oil with viscous dissipation over vertically moving surface: numerical and galerkin approach, Numer. Heat Transf. A: Appl. 86 (no. 2) (2025) 215–235.
[32] A.M. Obalalu, U. Khan, M.U. Hassan, M. Waqas, A.D. Adeshola, L. Ahmad, Electric double layer and thermal radiation effects on micropolar blood particles conveying Cu-MoS2-CuO nanoparticles in squeezed arterial channel, Nucl. Eng. Technol. 57 (8) (2025) 103604.
[33] G. Mandal, D. Pal, Dual solutions for magnetic-convective-quadratic radiative MoS2− SiO2/H2O hybrid nanofluid flow in Darcy-Fochheimer porous medium in presence of second-order slip velocity through a permeable shrinking surface: entropy and stability analysis, Int. J. Model Simul. 45 (no. 2) (2025) 517–543.
[34] K. Muhammad, M. Sarfraz, N. Ahammad, I.B.E. Elseesy, Improving thermal efficiency through Cu-MoS2 hybrid nanomaterials: a numerical and statistical approach, Chaos. Solit. Fractals 192 (2025) 116014.
[35] A.A. Faridi, N. Khan, K. Ali, M. Inc, Impact of magnetic induction on the flow of Maxwell hybrid nanofluid comprising of GO-TiO 2 and sodium alginate over a stretching sheet: a numerical study, Multiscale Multidiscip. Model Exp. Des. 8 (no. 5) (2025) 257.
[36] N.A.A. Jalil, S. Shafie, N.A.M. Noor, Chemical reaction impacts on squeezing radiative flow of sodium alginate-based casson ternary nanofluid with magnetohydrodynamics, Alex Eng. J. 114 (2025) 599–607.
[37] S.A. Lone, L.A.A. AL-Essa, F.S. Alduais, A. Al-Bossly, A. Dawar, A. Saeed, Optimization of heat transfer in bi-directional flow of sodium alginate-based ternary hybrid nanofluid over an extending heated surface with velocity slip conditions, J. Therm. Anal. Calorim. (2025) 1–12.
[38] C. Maheswari, B. Naga Lakshmi, R. Venkata Aravinda Raju, V.R. Kanuri, V. S. Bhagavan, M. Mohan Kumar, Thermal and radiative analysis on dynamics of ternary hybrid nanofluid accompanied by significance of viscous dissipation and magnetic field, J. Mines. Met. Fuels 73 (no. 5) (2025).
[39] K. Matarneh, U. Yashkun, R.I. Aldiabat, L.A. Lund, K. Fatima, Z. Shah, Ternary hybrid nanofluid flow and heat transfer characteristics in a permeable cylinder with viscous dissipation effect, Nanostruct. Nano-Objects 42 (2025) 101491.
[40] M. Ramzan, N. Shahmir, I. Alazman, C.V.A. Saleel, J.A.M. Asiri, A.M. Saeed, W. S. Koh, Heat transfer performance appraisal of hybrid and ternary nanofluid flows over a wedge considering viscous dissipation and quadratic thermal convection: non-similar solution approach, Adv. Mech. Eng. 17 (no. 6) (2025) 16878132251349955.
[41] Iqbal, Z., H. Xu, P.M. Parimala, X. Zhu, A.K. Hakeem, M.M. Alqarni, and R. Selmi. Viscous dissipation with suction/injection featuring the thermal enhancement of Cu–Fe3o4–Al2o3/water ternary hybrid nanofluid over a curved surface. MM Selmi Ridha Viscous Dissipation Suction/Inject. Featur. Therm. Enhanc. Cu 13Fe3o4 13Al2o3/Water Ternary Hybrid Nanofluid Curved Surf..
[42] Z. Abbas, I. Mahmood, S. Batool, S.A.A. Shah, A.D.E. Ragab, Evaluation of thermal radiation and flow dynamics mechanisms in the Prandtl ternary nanofluid flow over a Riga plate using artificial neural networks: a modified Buongiorno model approach, Chaos Solit Fractals 193 (2025) 116083.
[43] D.D. Ganji, M. Mahboobtosi, F.N. Chari, Three-dimensional flow analysis of penta and ternary-hybrid nanofluids over an elongating sheet with thermal radiation and gyrotactic microorganisms, Sci. Rep. 15 (no. 1) (2025) 24396.
[44] A.H.M. Galal, A. Anjum, S.S. Zafar, M. Faizan, A. Zaib, F. Ali, U. Khan, S. Elattar, S. M. Hussain, Computational assessment of chemically reactive tangent hyperbolic ternary hybrid nanofluid and thermal radiation in a Darcy-Forchheimer regime, J. Radiat. Res. Appl. Sci. 18 (no. 2) (2025) 101397.
[45] R. Cortell, Viscous flow and heat transfer over a nonlinearly stretching sheet, Appl. Math. Comput. 184 (no. 2) (2007) 864–873.
[46] K. Zaimi, A. Ishak, I. Pop, Boundary layer flow and heat transfer over a nonlinearly permeable stretching/shrinking sheet in a nanofluid, Sci. Rep. 4 (no. 1) (2014) 4404.